Journal of Computational Physics 448 (2022) 110737

Contents lists available at ScienceDirect

Journal of Computational Physics

www.elsevier.com/locate/jcp

Large Eddy Simulations by approximate weak entropy solutions

Magnus Svärd

Department of Mathematics, University of Bergen, Postbox 7800, 5020 Bergen, Norway

ARTICLE INFO

Article history:
Available online 11 October 2021

Keywords:
LES
Entropy solutions
Weak solutions
Stability

ABSTRACT

We propose to use weak (averaged) entropy solutions in lieu of LES models. This approach unites the theory for shock capturing schemes and turbulence modelling. To achieve this, we identify a number of conditions (albeit not sufficient) that a scheme should satisfy. Namely, a scheme should be: conservative, entropy dissipative, kinetic-energy preserving/diffusive, positivity preserving and have linearly stable (non anti-diffusive) continuity equation. We propose a finite-volume scheme with these properties and investigate its properties, and the properties of some related schemes, for the standard entropy-wave/shock interaction, a Kelvin-Helmoholtz instability, and a turbulent Rayleigh-Taylor problem.

These preliminary investigations suggest that the scheme is very robust, is competitive for turbulent problems and is far less prone to trip false turbulence. However, and as with any general purpose scheme, wildly under-resolved simulations can not be expected to be accurate. The advantage with the current scheme is that local averages converge which provides a possibility to estimate the accuracy of functionals of interest.

1. Introduction

The compressible Navier-Stokes equations take the form,

$$\begin{aligned} \partial_t \rho + div(\rho \mathbf{v}) &= 0 \\ \partial_t(\rho \mathbf{v}) + div(\rho \mathbf{v} \otimes \mathbf{v}) + \nabla p &= div \mathbb{S}, \qquad \mathbf{x} \in \Omega \\ \partial_t(E) + div(E\mathbf{v} + p\mathbf{v}) &= div \mathbb{S}\mathbf{v} + div(\kappa \nabla T) \\ p &= \rho R T \quad \text{ideal gas law} \end{aligned} \tag{1}$$

where $\mathbf{x} = (x, y, z)$ and Ω is the periodic unit box. Moreover, $E = \frac{1}{2}\rho|\mathbf{v}|^2 + \rho e$ is the total energy; $e = c_v T$ is the internal energy and T the temperature; $\rho e = \frac{p}{\gamma - 1}$, where ρ and p are the density and pressure. $\mathbf{v}^T = (u, v, w)$ are the Cartesian velocity components. Furthermore, the adiabatic exponent $\gamma = c_p/c_v$ and R is the gas constant. The stress tensor is given by: $(\mathbb{S})_{ij} = \tau_{ij} = -\frac{2}{3}\mu v_{k,k}\delta_{ij} + \mu(v_{i,j} + v_{j,i}) + \eta v_{k,k}\delta_{ij}$. The equations (1) are stated on the so-called conservative form and we refer to the variables, $\mathbf{u} = (\rho, \rho\mathbf{v}^T, E)^T$ as conservative. We consider constant dynamic viscosity $\mu = \mu_0 > 0$ and

E-mail address: Magnus.Svard@uib.no.

https://doi.org/10.1016/j.jcp.2021.110737

bulk viscosity $\eta = 0$. To obtain strong bounds on temperature, we consider heat conductivities, κ, with $\kappa_0(1 + T^p) \leq \kappa \leq \kappa_1(1 + T^p)$ where $\kappa_{0,1}$ are constants and p is an appropriately large integer. (We will use $p = 2$ as an example.)

The great variety of phenomena that solutions of the Navier-Stokes equations display and the inability to fully resolve the solutions in numerical simulations of engineering problems, have spawned research in a multitude of directions. Two important fields within computational fluid dynamics focus on approximations of shock solutions and turbulence modelling. Herein, we consider entropy-stable shock schemes designed to approximate weak entropy solutions (see e.g. [2,21]) and Large Eddy Simulations (LES) (see e.g. [9,15]).

Very briefly, in LES a filter is applied to (1) a priori, leading to a new system that is closed by modelling turbulent diffusion. On the other hand, weak solutions satisfy the weak form of (1) and should at least be accurate in an averaged way, which is akin to a posteriori filtering.

The main objective of this paper is to identify conditions that a numerical scheme should satisfy in order to allow an LES interpretation of its solutions. The secondary objective is to derive such a scheme and evaluate its performance. Hence, we begin by detailing the concept of weak solutions and their use when designing shock-capturing schemes, as well as the basic principles of LES. The remainder of the paper is devoted to analysis leading to a finite volume/difference scheme for the Navier-Stokes equations. The proposed scheme is subsequently tested for the Shu-Osher shock/entropy-wave interaction, a Kelvin-Helmholtz instability and a Taylor-Green vortex.

Throughout, we assume that there exists a weak solution to the Navier-Stokes equations for reasonably general (say piecewise smooth) initial and boundary data.

Furthermore, we assume that admissible weak solutions depend continuously on data. That is, the limit of any weakly convergent sequence of numerical solutions should be independent of the particular numerical scheme and choices of grids used to produce it. Therefore, we require that dynamic instabilities, in grid converged solutions, are tripped by user provided data and not by numerical errors. (In fact, it suffices that local averages are continuous with respect to data for the discussion below.)

Before proceeding we make some further comments on the type of solutions that may or may not exist. We have chosen to frame the discussion around weak entropy solutions. We stress that it is not known if the Navier-Stokes equations admit such solutions. In [6], a form of weak solution was proven to exist but not with the standard ideal gas law. Another form of weak solution was established in [8] for yet another, non-standard, version of the Navier-Stokes system. For the standard Navier-Stokes systems it may well be that weak solutions do not exist and dissipative measure-valued solutions is the correct notion of solutions, as demonstrated in [7] under some fairly strong assumptions.

However, this does not change the current discussion in any significant way, as the purpose is *not* to prove convergence to either form of solutions but investigate averages on coarse meshes and relate those to an LES interpretation.

2. Basic concepts and main idea

2.1. Weak entropy solutions

For brevity, we use the viscous Burgers equation on the real line as a prototype for (1) when introducing the concepts. It takes the form

$$\mathtt{u}_t + (\mathtt{f}(\mathtt{u}))_x = \nu \mathtt{u}_{xx}, \quad \nu > 0, \quad x \in \mathbb{R}, \quad t \in [0, \mathcal{T}], \tag{2}$$

where $\mathtt{f}(\mathtt{u}) = \frac{\mathtt{u}^2}{2}$ and ν a viscosity parameter. We assume that initial data is compactly supported and bounded, and seek a weak (distributional) solution. That is, $\mathtt{u}$ satisfies

$$\int \phi \mathtt{u}|_{t=0}\, dx + \int \phi_t \mathtt{u}\, dx\, dt + \int \phi_x \mathtt{f}(\mathtt{u})\, dx\, dt = \int \phi_x \nu \mathtt{u}_x\, dx\, dt \tag{3}$$

for any smooth and compactly supported $\phi(x, t) \in C_0^\infty([0, \infty) \times \mathbb{R})$. To derive a priori estimates, we can assume that the solution is appropriately smooth. Multiplying (2) by $\mathtt{u}$, we obtain an equation for the entropy $\mathtt{u}^2/2$,

$$\partial_t(\frac{\mathtt{u}^2}{2}) + \partial_x(\frac{\mathtt{u}^3}{3}) = \nu(\mathtt{u}\mathtt{u}_x)_x - \nu \mathtt{u}_x^2 \tag{4}$$

Integrating in space and assuming compact support of $\mathtt{u}$, result in the global entropy balance,

$$\partial_t \int \frac{\mathtt{u}^2}{2}\, dx + \int \nu \mathtt{u}_x^2\, dx = 0, \tag{5}$$

and the bounds,

$$\mathtt{u} \in L^\infty(0, \mathcal{T}; L^2(\mathbb{R})),$$
$$\mathtt{u} \in L^2(0, \mathcal{T}; H^1(\mathbb{R})).$$

Assuming that we have a sequence of approximate solutions satisfying these estimates (and drawing subsequences where necessary), we can use Aubin-Lions Lemma (see e.g. [18]) to obtain compactness and pointwise convergence of $\mathtt{u}$. By Sobolev embedding and a standard interpolation inequality (see Appendix of [4]), we have $\mathtt{u} \in L^{10/3}(0,\mathcal{T};L^{10/3}(\mathbb{R}))$, which along with pointwise convergence implies weak convergence of $\mathtt{u}^2 \in L^{5/3-\epsilon}(0,\mathcal{T};L^{5/3-\epsilon}(\mathbb{R}))$, $\epsilon>0$. The H^1 estimate also implies weak convergence of the diffusive term. Hence, a subsequence converges to a weak solution of (2).

However, these estimates are not sufficient for weak convergence of (4), but the following inequality is weakly satisfied:

$$\partial_t(\frac{\mathtt{u}^2}{2})+\partial_x(\frac{\mathtt{u}^3}{3})\leq 0, \tag{6}$$

since u^3 is weakly convergent in $L^{1+\epsilon}(0,\mathcal{T};L^{1+\epsilon}(\mathbb{R}))$ for some $\epsilon>0$. We term solutions that, in the weak sense, satisfy (2) and (6) as *weak entropy solutions*.

Clearly a numerical scheme must satisfy the same a priori estimates to converge weakly. (For convex and scalar conservation laws, one can go further and prove that the solution is strong, i.e., it satisfies (2), and is unique. See e.g. [17].)

Remark. Unlike linear problems, mere boundedness of the numerical solution, e.g. in $L^\infty(0,T;L^2(\mathbb{R}))$, is not sufficient for convergence. △

Remark. Note that the above arguments actually imply that a subsequence of $\mathtt{u}$ converges *strongly* in $L^{10/3-\epsilon}(0,\mathcal{T},L^{10/3-\epsilon})$, $\epsilon>0$. For the Navier-Stokes equations, convergence to a weak solution would require that the primary variables converge strongly. However, and as will be discussed below, it is averages of $\mathtt{u}$ that can be likened to LES and hence it is the weak convergence of $\mathtt{u}$ that we focus on.

2.2. Large Eddy Simulation

In LES, the Navier-Stokes equations are convolved with a low-pass filter of a certain width Δ. Using (2) as a prototype, we have

$$\int \Phi_\Delta(x-r)\mathtt{u}(r,t)_t\,dr+\int \Phi_\Delta(x-r)\mathtt{f}(\mathtt{u}(r,t))_x\,dr=\int \nu\Phi_\Delta(x-r)\mathtt{u}(r,t)_{xx}\,dr$$

By defining $\bar{\mathtt{u}}(x,t)=\int \Phi_\Delta(x-r)\mathtt{u}(r,t)\,dr=\Phi_\Delta*\mathtt{u}$ and assuming that the filter operator and differentiation commute (see e.g. [14]), the linear terms can be recast as,

$$\begin{aligned}\Phi_\Delta*\mathtt{u}_t&=\partial_t\bar{\mathtt{u}}(x,t),\\ \nu\Phi_\Delta*\mathtt{u}_{xx}&=\nu\partial_{xx}\bar{\mathtt{u}}.\end{aligned}$$

The non-linear flux $\mathtt{f}(\mathtt{u})$, is the main challenge. Formally, one obtains,

$$\int \Phi_\Delta(x-r)\mathtt{f}(\mathtt{u}(r,t))_x\,dr=\mathtt{f}(\bar{\mathtt{u}}(x,t))_x-\mathtt{R}$$

where the remainder, $\mathtt{R}$, requires knowledge of the effect of turbulent fluctuations. On average, $\mathtt{R}$ should effectuate turbulent mixing and is therefore commonly modelled as a turbulent diffusion $(\nu_T\bar{\mathtt{u}}_x)_x$. The viscous conservation law, (2) is then replaced by,

$$\bar{\mathtt{u}}_t+\mathtt{f}(\bar{\mathtt{u}})_x=((\nu+\nu_T)\bar{\mathtt{u}}_x)_x, \tag{7}$$

where ν_T requires some further modelling. We emphasise that with a fixed Δ, the grid converged numerical solution solves (7), *not* (2). Ideally, ν_T should be chosen such that the application of the same filter on the solution $\mathtt{u}$ of (2), yields the solution of (7). This is the main challenge of LES since it ultimately requires a priori knowledge of the scales removed by the filter.

Remark. For (1), the turbulent diffusion is often modelled by the Smagorinsky model

$$\nu_T\mathbb{S}=(c_s\Delta^2)|\bar{\mathbb{S}}|\bar{\mathbb{S}}, \tag{8}$$

where c_s is a model parameter. See e.g. [13] for LES of compressible flows. △

To obtain numerical solutions with higher fidelity, the Δ in the LES model is often taken to be proportional to the grid cell diameter (h). This is also referred to as LES although it is fundamentally different. With such an approach $\nu_T\to 0$ as $h\to 0$; $(\nu_T\mathtt{u}_x)_x$ becomes a vanishing viscosity term and a convergent solution solves (2), not (7). We refer to this as *vanishing LES*. Solutions of (2) correspond to DNS (Direct Numerical Simulations) solutions of (1).

Another technique, referred to as Implicit LES (ILES), uses the built-in numerical artificial diffusion as an LES model. The rationale for this approach is that the truncation errors of a numerical scheme can (sometimes) be viewed as the residuals of a filtering procedure; see [1]. Also for ILES, a convergent numerical solution solves (2).

In general, there are no strong reasons to assume that neither vanishing LES (with $\Delta \sim h$) nor ILES produce approximations that converge to a DNS solution. Convergent schemes have to satisfy a suite of a priori estimates, which impose severe restrictions on numerical schemes. (See e.g. [6] and below.)

Our aim is to propose a general purpose method that does not require explicit subgrid-scale modelling. Hence, we do not consider LES models with a fixed filter width. The scheme herein could be viewed as ILES, although the rationale is fundamentally different, but its solutions are interpreted in a sense similar to a fixed-width LES.

2.3. LES interpretation of weak solutions

A numerical scheme approximating weak solutions, discretises the original equations (2) (or (1)). However, its solutions can not be expected to satisfy the equations pointwise.

Let $\{x_i\}$, $i = 0, \pm 1, \pm 2, \dots$ be the discretisation of the real axis with grid spacing h. Let $\mathbf{\Phi}$ be the grid function obtained by projecting a test function, ϕ, onto the grid, such that the ith component is given by $[\mathbf{\Phi}]_i = \Phi_i = \phi(x_i)$. Suppose that we have a weakly convergent sequence of numerical approximations $\mathbb{U}^h$ (a grid function on the grid with spacing h). That is,

$$\lim_{h\to 0} \sum_i (\Phi_i)^T \mathbb{U}_i^h h = \int \phi u \, dx \tag{9}$$

for any (fixed) test function ϕ. $\mathbf{\Phi}$ denotes the grid-function obtained by projecting ϕ onto the grid.

Remark. In a system of conservation laws, the choice of test functions may differ for different variables. We assume that we at least have convergence when $\phi \in C_0^\infty([0,\infty) \times \mathbb{R})$. Furthermore, a weak solution is typically averaged in time as well. For brevity, we drop the averaging in time in the discussion below.

We give an example to shed further light on this type of convergence. Consider a grid with spacing H. Choose a test function $\mathbf{\Phi}$ whose support coincides with cell i. (This requires some further justifications, which we omit for brevity, as this would be an indicator function which is not smooth.) For such a function, $(\mathbf{\Phi}, \mathbb{U}^H) = \mathbb{U}_i^H V_i$ where V_i is the measure of the length of cell i. However, if we make a grid refinement such that $h = H/2$. Then the original cell i would consist of *two* cells on the finer grid. Let these cells have indices, j, $j+1$, then $(\mathbf{\Phi}, \mathbb{U}^h) = \mathbb{U}_j^h V_j + \mathbb{U}_{j+1}^h V_{j+1}$. Further refinements would involve more points and it is this quantity that we assume converges.

Remark. Convergence of point values amounts to changing Φ between each grid refinement such that its support only encompasses the point in question. We do not assume that such sequences converge, although they may in regions where the solution is smooth. $\triangle$

Turning to a grid with a finite $h > 0$, the accuracy of the approximation of the integral $(\mathbf{\Phi}, \mathbb{U}^h)$, depends, not only on the accuracy of the numerical approximation $\mathbb{U}^h$, but on the resolution of $\mathbf{\Phi}$. In principle, the larger support of $\mathbf{\Phi}^h$ the more accurate the integral approximation is for finite $h > 0$ (and the closer to converged it probably is). Clearly, if $\mathbf{\Phi} = 1$ on the support of $\mathbb{U}$, it is the conservation statement which is exactly satisfied for any h. Conversely, a single cell value, $\mathbb{U}_i$, represents (9) where $\mathbf{\Phi}$ is the unit top-hat function with support on the cell i, which is very under-resolved. In general, neither single-cell values, nor the average of a few points, can be expected to accurately represent the solution in oscillatory regions or for massively under-resolved solutions.

However, the advantage with the weak-solution approach, is that if the scheme is convergent, the functional of interest provides some information about the resolution requirements. In practice, we would simply grid refine until we have a sufficiently small change of the integral we are interested in. (This may or may not require resolution of all scales of the solution.) *In many cases, less than full resolution will be required to obtain sufficiently accurate functionals/averages. This is the LES interpretation of weak solutions.*

Remark. As already mentioned, convergence to a weak solution, requires strong convergence of the primary variables in L^p for p suitably large. However, our aim is to make an LES interpretation of the solution on coarse meshes and not investigate the convergence as $h \to 0$. It stands to reason that averages on large enough subdomains will display convergence earlier, i.e. on coarser meshes, than the strongly convergent sequences do. $\triangle$

Finally, we remark that although this approach is similar to ILES in that the solution converges weakly to the DNS solution, its weak interpretation is somewhat similar to LES with a fixed filter width, since the test function in any converging sequence $(\mathbf{\Phi}, \mathbb{U}^h)$ has a fixed support as $h \to 0$. However, unlike fixed-width LES, the fixed support can be chosen to be arbitrarily small (if h is adequately smaller).

3. Identifying necessary conditions

Although the theory of weak solutions of (1) is incomplete, it is clear that, as in the scalar case, strong estimates on all principal variables, $\rho, \mathbf{v}, T$, are necessary. Here, we briefly discuss some, albeit insufficient, estimates. Since our goal is weak convergence, we conjecture that a numerical scheme should (at least) satisfy the corresponding discrete estimates.

From conservation and by assuming positivity, the following bounds follow from direct integration of the continuity and energy equation of (1):

$$\rho,\ E,\ \rho|\mathbf{v}|^2,\ p \in L^\infty(0,\mathcal{T};L^1(\Omega)). \tag{10}$$

The entropy function is defined as $U = -\frac{\rho S}{\gamma-1}$, where $S = \log(\frac{p}{\rho^\gamma})$ is the specific entropy. By recasting (1) as a transport equation for U, integrating in space and time, and using (10), one obtains the following bounds from the diffusive terms,

$$\int_0^{\mathcal{T}}\int_\Omega \left(\frac{\mu}{R}\frac{|\nabla\mathbf{v}|^2}{T} + \frac{\kappa}{R}\frac{|\nabla T|^2}{T^2}\right) d\mathbf{x}\,dt \le \mathcal{C}$$

where $\mathcal{C}$ denotes a constant depending on initial data. With $\kappa \sim (1+T^2)$, we have the bounds

$$\begin{aligned} \nabla\log(T) &\in L^2(0,\mathcal{T};L^2(\Omega)), \\ \nabla T &\in L^2(0,\mathcal{T};L^2(\Omega)). \end{aligned} \tag{11}$$

Remark. $\kappa = constant$ gives only the first bound of (11), which is not sufficient to bound the heat flux. Hence, a temperature dependent κ is required. △

The log-bound of temperature can be used to demonstrate positivity of temperature (if we have made sure that ρ remains positive, see [8]) and one can infer, using a Poincare inequality, that

$$\begin{aligned} T &\in L^2(0,\mathcal{T};H^1(\Omega)), \\ T &\in L^2(0,\mathcal{T};L^6(\Omega)), \end{aligned}$$

where the last bound follows from Sobolev embedding.

Furthermore, by subtracting the kinetic energy balance from the total energy equation, the internal energy equation is obtained from which stronger bounds on temperature and ultimately $|\nabla\mathbf{v}|$ can be obtained. (We refer to [8] for further details on a priori estimates.) Although these estimates have not been shown to produce weak solutions, they are part of theory demonstrating weaker forms of solutions (see [6]), which is our rationale for demanding that a numerical scheme should behave similarly.

To mimic the above estimates, a numerical scheme should:

- **A.** be on divergence form (conservation form) to provide the discrete estimates (10).
- **B.** bound the entropy to give the temperature bounds (11).
- **C.** be equal or more diffusive than *kinetic energy preserving* fluxes, as they are defined in [3]. This allows a discrete kinetic energy balance and an internal energy balance, which in turn yield estimates on velocity and temperature.
- **D.** guarantee a non-negativite density, which along with the log-estimate of temperature, guarantee non-negativity of ρ, p and T.

Remark. To clarify Condition C: The notion "Kinetic-energy preserving flux" refers to the discretisation of the inviscid fluxes and such fluxes do not artificially diffuse the discrete kinetic energy balance. However, we allow the approximation of inviscid fluxes to contain artificial viscosity that diffuses kinetic energy. Furthermore, the physical diffusion in the Navier-Stokes equations also diffuses kinetic energy.

Remark. Since these conditions are insufficient, the list above is preliminary. Furthermore, these conditions would have been necessary, had we framed the discussion around measure-valued solutions. △

Next, we briefly discuss various aspects and choices that ultimately takes us to the scheme we propose to use to approximate weak solutions of (1). To this end, we consider a generic equidistant finite-volume scheme for the 1-D (one-dimensional) version of (1).

$$(\mathbf{u}_i)_t + \frac{\mathbf{f}^I(\mathbf{u}_{i+1/2}) - \mathbf{f}^I(\mathbf{u}_{i-1/2})}{h} = \frac{\mathbf{f}^V_{i+1/2} - \mathbf{f}^V_{i-1/2}}{h}, \tag{12}$$

where $\mathbf{f}^I_{i+1/2}$ and $\mathbf{f}^V_{i+1/2}$ are the inviscid and viscous flux approximations. Clearly, Condition A is satisfied for (12) (which is standard for shock-capturing schemes).

To shed some light on the non-negativity of ρ (Condition D), we consider the simplest possible flux

$$\mathbf{f}^I_{i+1/2} = \frac{\mathbf{f}^I(\mathbf{u}_{i+1}) + \mathbf{f}^I(\mathbf{u}_i) - \lambda_{i+1/2}(\mathbf{u}_{i+1} - \mathbf{u}_i)}{2} \tag{13}$$

where $\mathbf{f}^I(\mathbf{u}_i) = (\rho u, \rho u^2 + p, u(E+p))_i$. Then the continuity equation takes the form,

$$(\rho_i)_t + \frac{(\rho u)_{i+1/2} - \frac{\lambda_{i+1/2}}{2}\Delta\rho_{i+i/2} - ((\rho u)_{i-1/2} - \frac{\lambda_{i-1/2}}{2}\Delta\rho_{i-1/2})}{h} = 0 \tag{14}$$

where $\Delta\rho_{i+1/2} = \rho_{i+1} - \rho_i$ and $(\rho u)_{i+1/2} = ((\rho u)_{i+1} + (\rho u)_i)/2$. We rewrite (14)

$$(\rho_i)_t = \frac{-\rho_{i+1}(u_{i+1} - \lambda_{i+1/2}) - (\lambda_{i+1/2} + \lambda_{i-1/2})\rho_i + \rho_{i-1}(u_{i-1} + \lambda_{i-1/2})}{2h}. \tag{15}$$

If $\lambda_{i+1/2} \geq \max(|u_i|, |u_{i+1}|)$ for all i, the scheme is non-negative since $\rho_i \to 0$ implies $(\rho_i)_t \geq 0$.

Clearly, Rusanov's flux (local Lax-Friedrichs), where $\lambda_{i+1/2} = \max(|u_i| + c_i, |u_{i+1}| + c_{i+1})$ (where c_i is the sound speed), satisfies the positivity Condition D and in [21] it is also shown to be entropy stable, i.e., Condition B. (We also emphasise that $\mathbf{f}^V_{i+1/2}$ has to be chosen appropriately for the full Navier-Stokes equations to be entropy stable. See e.g. [16].)

However, E-schemes (that are stable with respect to all entropies, such as Rusanov) are very diffusive and generally considered inappropriate for turbulent simulations. A seemingly better choice is an *entropy conservative* approximation of $\mathbf{f}_{i+1/2}$, e.g., [12] or [3], that satisfies Condition B and can be extended to high formal accuracy. (See [5].) The entropy conservative flux derived in [3] also preserves kinetic energy. It checks Conditions A-C and appears to be a very promising candidate for our scheme. (We will refer to this as Chandrashekar's flux.)

Unfortunately, schemes based on entropy conservative fluxes are not locally linearly stable in the sense discussed in [10]. In the inviscid case, the neutrally linearly stable approximation of (12) was shown to be the central non-diffusive central flux given by

$$\mathbf{f}^I_{i+1/2} = \frac{\mathbf{f}^I(\mathbf{u}_{i+1}) + \mathbf{f}^I(\mathbf{u}_i)}{2}.$$

Clearly, inviscid fluxes of the form (13) are linearly stable when $\lambda_{i+1/2} \geq 0$. (However, the viscous and heat conductive flux, $\mathbf{f}^V_{i+1/2}$, also contributes to linear stability and allows other forms of inviscid fluxes.)

The problem with local linear instabilities is that numerical errors may be artificially amplified. (Examples of this were given in [10].) If this happens in a region where there is a dynamic instability, the linear instability may develop a sufficiently large disturbance such that it erroneously trips the dynamic instability and causes the solution to bifurcate into an unphysical (erroneous) solution. (For instance, it could trip unphysical turbulence.) This is not consistent with the well-posedness requirement that solutions are continuous with respect to input data

Remark. As shown in [10], a scheme that is non-linearly, but not linearly, stable, does not blow up. Hence, one can not take for granted that a bounded numerical solution is an approximation of the true solution. △

As mentioned above, the physical diffusion provides some control on velocity and temperature gradients, whilst there is no control of density gradients. (This is an immediate consequence of the hyperbolic-parabolic character of (1).) Hence, we add the following linear stability condition.

E. The scheme for the continuity equation must be linearly stable (non anti-diffusive).

Finally, we wish the scheme to be as accurate as possible. Hence, we strive to add as little extra diffusion as possible.

3.1. Subgrid-scale model

Before turning to the construction of a scheme satisfying Conditions A-E, we comment the conditions in the context of subgrid-scale modelling.

First, the entropy condition (B) is reasonable for an LES model as well. Whatever the solution is at the subgrid scale, that LES is trying to model, it does not violate the Second Law of Thermodynamics. However, in LES ν_T is typically not deliberately chosen to satisfy a discrete entropy condition.

Furthermore, LES (with fixed Δ) has to be Galilean invariant which is satisfied by $\nu_T \sim |\mathbb{S}|$ as in (8). With our approach, the artificial diffusion plays the role of subgrid-scale model and in the previous Section it was indicated $\lambda_{i+1/2}$ has to scale with the velocity to ensure positivity. This does not violate Galilean invariance, since $\lambda_{i+1/2}$ is a vanishing viscosity

coefficient and the corresponding flux approximation (13) is consistent with the inviscid flux of (1). (It is only for fixed width LES that attention to Galilean invariance is required.)

Next, we take a closer look at (8) where $\nu_T \sim |\mathbb{S}|$. By a scaling argument one obtains $\nu_T \sim l_T u_T$ where l_T is the turbulent length scale and u_T the scale of turbulent velocity fluctuations. Thus, in (8), $u_T \sim l_T |\nabla \tilde{\mathbf{v}}|$ and $l_T \sim \Delta$.

If we instead consider a grid cell of size h in a 3-D Cartesian equidistant grid, the unresolved turbulent length scale is $l_T \sim h$. Assuming that we know the exact solution, we may calculate the surface integral giving the mass influx to the cell. On a cell face it would be equal to $\overline{\rho \mathbf{v} \cdot \mathbf{n}} h^2$ (where $\mathbf{n}$ is the outward unit normal and the overbar denotes the average). Numerically, we could approximate the integral by, for instance, the upwind flux. This gives the standard upwind scheme which is positive according to (15) and corresponds to (14) with $\lambda_{i+1/2} = \max(|u_i|, |u_{i+1}|)$. If $\lambda_{i+1/2}$ is interpreted as ν_T, it amounts to $(\nu_T)_{i+1/2} \sim h \max(|u_i|, |u_{i+1}|)$. In this view, u_T is proportional to the mean velocity. Furthermore, it leads to the turbulent cell Reynolds number

$$(Re_h)_i = \frac{u_i h}{\nu_T} \sim 1$$

which seems like a reasonable scaling, if the extra viscosity is meant to diffuse subgrid-scale structures. Our point is that upwind-type schemes, where $\lambda \sim |u_i|$, can not be ruled out as subgrid-scale models.

4. A scheme for moderately under-resolved solutions

In this section, we design a scheme for (1) satisfying the Conditions A-E. The inviscid terms pose the main challenge, and they are essentially one-dimensional. Hence, we carry out the analysis in 1-D to reduce notation.

We discretise the periodic domain, Ω, with equidistant grid spacing h and number the points as $x_0, ..., x_N$, where x_0 and x_N represent the same point. (For brevity, we omit the statements of the scheme at boundaries where the obvious mappings of points are tacitly assumed.) We also need the following definitions:

$$\begin{aligned}
\bar{a}_{i+1/2} &= \frac{a_{i+1} + a_i}{2}, \\
\Delta a_{i+1/2} &= a_{i+1} - a_i, \\
\hat{a}_{i+1/2} &= \frac{\Delta a_{i+1/2}}{\Delta \log(a)_{i+1/2}}, \quad \text{(log mean)}, \\
\check{a}_{i+1/2} &= \sqrt{a_i a_{i+1}} \quad \text{(geometric mean)}, \\
D_- a_p &= \frac{a_p - a_{p-1}}{h}
\end{aligned} \tag{16}$$

and the identities,

$$\begin{aligned}
\Delta(ab)_{i+1/2} &= \bar{a}_{i+1/2} \Delta b_{i+1/2} + \bar{b}_{i+1/2} \Delta a_{i+1/2} \\
\overline{(ab)}_{i+1/2} &= \bar{a}_{i+1/2} \bar{b}_{i+1/2} + \frac{1}{4} \Delta b_{i+1/2} \Delta a_{i+1/2}.
\end{aligned} \tag{17}$$

Furthermore, the discrete L^2-equivalent norm for a grid function $\mathtt{a}$, is given by,

$$\|\mathtt{a}\|_2^2 = \sum_{i=1}^{N} h a_i^2. \tag{18}$$

As discussed above, Chandrashekar's entropy-conserving and kinetic-energy preserving inviscid flux ([3]) has many of the desired properties and we modify it to obtain a scheme that satisfies all Conditions A-E. Hence, we use Chandrashekar's notation and define

$$\beta = \frac{1}{2RT}. \tag{19}$$

Let

$$(\mathbf{u}_i)_t + \frac{\mathbf{f}_{i+1/2} - \mathbf{f}_{i-1/2}}{h} = 0 \tag{20}$$

be the 1-D Navier-Stokes equations, where $\mathbf{u}_i = (\rho_i, m_i, E_i)^T$, i.e., density, momentum and total energy. Furthermore, $\mathbf{f}^I_{i+1/2} = (f^\rho, f^m, f^E)^T_{i+1/2}$, $\mathbf{f}^V_{i+1/2} = (f^{V1}, f^{V2}, f^{V3})^T_{i+1/2}$ and $\mathbf{f}_{i+1/2} = \mathbf{f}^I_{i+1/2} + \mathbf{f}^V_{i+1/2}$ is the sum of the inviscid and viscous (and heat conductive) fluxes. The fluxes are given by

$$
\begin{aligned}
f^{\rho}_{i+1/2} &= \bar{\rho}_{i+1/2}\bar{u}_{i+1/2} - \lambda^{\rho}_{i+1/2}\Delta\rho_{i+1/2} \\
f^{m}_{i+1/2} &= \frac{\bar{\rho}_{i+1/2}}{2\bar{\beta}_{i+1/2}} + \bar{u}_{i+1/2}\mathbf{f}^{\rho}_{i+1/2} = \tilde{p}_{i+1/2} + \bar{u}_{i+1/2}\mathbf{f}^{\rho}_{i+1/2} \\
f^{E}_{i+1/2} &= \left(\frac{1}{2(\gamma-1)\hat{\beta}_{i+1/2}} - \frac{1}{2}\overline{u^2}_{i+1/2} \right) \mathbf{f}^{\rho} + \bar{u}_{i+1/2}\mathbf{f}^{m}
\end{aligned}
\tag{21}
$$

where,

$$
\lambda^{\rho}_{i+1/2} = \frac{|\bar{u}_{i+1/2}|}{2} + \frac{|\Delta u_{i+1/2}|}{4},
\tag{22}
$$

and

$$
\begin{aligned}
f^{V1}_{i+1/2} &= 0 \\
f^{V2}_{i+1/2} &= (\tau_{xx})_{i+1/2} = \frac{4}{3}\mu\frac{u_{i+1}-u_i}{h} \\
f^{V3}_{i+1/2} &= \bar{u}_{i+1/2}(\tau_{xx})_{i+1/2} + \kappa_{i+1/2}\frac{T_{i+1}-T_i}{h}
\end{aligned}
\tag{23}
$$

and $\kappa_{i+1/2} = \bar{\kappa}_{i+1/2}$.

Remark. Before we proceed and prove that the proposed Euler flux have the desired properties A-E, we point out that the flux (21) is not unique. We could equally well have chosen,

$$
f^{\rho}_{i+1/2} = \overline{\rho u}_{i+1/2} - \lambda^{\rho}_{i+1/2}\Delta\rho_{i+1/2}
\tag{24}
$$

in (21). It is straightforward to show that this flux also satisfies the desired properties by slightly modifying the proofs below. (Interestingly, both versions require the same artificial viscosity, λ^{ρ}, for the proofs to hold.) We have tried both fluxes in numerical experiments and the two appear to be very similar. We proceed with (21). △

Clearly, using (21) in (20) results in an approximation of the divergence form implying that A is satisfied. Next, we recast the convective mass flux $\mathbf{f}^{\rho}$ using (17) as

$$
\mathbf{f}^{\rho}_{i+1/2} = \overline{\rho u}_{i+1/2} - (\lambda^{\rho}_{i+1/2} + \frac{1}{4}\Delta u_{i+1/2})\Delta\rho_{i+1/2}
\tag{25}
$$

and note that $\lambda^{\rho}_{i+1/2} + \frac{1}{4}\Delta u_{i+1/2} \geq 0$. That is, the mass equation is on standard form with artificial diffusion. The two remaining variables are, at least for $h > 0$ small enough, diffused by the physical diffusion terms. Hence, the scheme is locally linearly stable in the sense of ([10] and satisfies Condition E.

Turning to positivity (Condition D), we require that $(\rho_i)_t \geq 0$ when $\rho_i \to 0^+$. Hence, we calculate,

$$
\lim_{\rho_i\to 0^+}(f^{\rho}_{i+1/2} - f^{\rho}_{i-1/2}) =
$$

$$
\lim_{\rho_i\to 0^+}\left(\bar{\rho}_{i+1/2}\bar{u}_{i+1/2} - \lambda^{\rho}_{i+1/2}\Delta\rho_{i+1/2} - \left(\bar{\rho}_{i-1/2}\bar{u}_{i-1/2} - \lambda^{\rho}_{i-1/2}\Delta\rho_{i-1/2}\right)\right) =
$$

$$
\rho_{i+1}\frac{1}{2}\bar{u}_{i+1/2} - \lambda^{\rho}_{i+1/2}\rho_{i+1} - \left(\rho_{i-1}\frac{1}{2}\bar{u}_{i-1/2} + \lambda^{\rho}_{i-1/2}\rho_{i-1}\right) < 0
$$

where the last inequality follows from $\lambda^{\rho}_{i+1/2} > \frac{1}{2}|\bar{u}_{i+1/2}|$. We conclude that (20) ensures positivity of density, i.e., satisfies Condition D.

To demonstrate entropy stability, we note that $U = -\frac{\rho S}{\gamma-1}$ is the only entropy function for the Navier-Stokes equations. (See [11].) (Note the sign change: U must not increase according to the Second Law of Thermodynamics.) $F = -\frac{\rho u S}{\gamma-1} = uU$ is the entropy flux and $\Psi = m = \rho u$ the entropy potential. Furthermore,

$$
\mathbf{w}^T = U_{\mathbf{u}} = \left(\frac{\gamma - S}{\gamma - 1} - \beta u^2, 2\beta u, -2\beta\right),
\tag{26}
$$

are the entropy variables.

Next, we multiply (20) by the entropy variables $h\mathbf{w}_i^T$ and carry out some standard manipulations (see [21]) to obtain,

$$\begin{aligned} &hU(\mathbf{u}_i)_t + \mathbf{F}_{i+1/2} - \mathbf{F}_{i-1/2} \\ &-\frac{1}{2}\left(\Delta w_{i+1/2}^T \bar{\mathbf{f}}_{i+1/2}^I - \Delta\Psi_{i+1/2} + \Delta w_{i-1/2}^T \bar{\mathbf{f}}_{i-1/2}^I - \Delta\Psi_{i-1/2}\right) = \\ &\bar{\mathbf{w}}_{i+1/2}^T \mathbf{f}_{i+1/2}^V - \frac{1}{2}\Delta\mathbf{w}_{i+1/2}^T \mathbf{f}_{i+1/2}^V - \bar{\mathbf{w}}_{i-1/2}^T \mathbf{f}_{i-1/2}^V - \frac{1}{2}\Delta\mathbf{w}_{i-1/2}^T \mathbf{f}_{i-1/2}^V, \end{aligned}$$

where

$$\mathbf{F}_{i+1/2} = \bar{\mathbf{w}}_{i+1/2}^T \bar{\mathbf{f}}_{i+1/2}^I - \bar{\Psi}_{i+1/2}, \tag{27}$$

is the numerical entropy flux. Upon summation in space, where the conservative terms telescope and vanish, it is clear that the entropy is bounded from above if

$$\Delta\mathbf{w}_{i+1/2}\mathbf{f}_{i+1/2}^V \geq 0 \quad \forall i \tag{28}$$

and Tadmor's shuffle condition (see [21]),

$$\Delta\mathbf{w}_{i+1/2}^T \bar{\mathbf{f}}_{i+1/2}^I \leq \Delta\Psi_{i+1/2} \quad \forall i \tag{29}$$

are both satisfied. (Fluxes satisfying (29), are termed entropy stable, or entropy conservative in case of equality.)

We begin by showing that (29) holds. In [3] the following expressions were derived,

$$\begin{aligned} \Delta\mathbf{w}_1 &= \frac{\Delta\rho}{\hat{\rho}} + \left(\frac{1}{(\gamma-1)\hat{\beta}} - \overline{u^2}\right)\Delta\beta - 2\bar{u}\bar{\beta}\Delta u, \\ \Delta\mathbf{w}_2 &= 2\bar{\beta}\Delta u + 2\bar{u}\Delta\beta, \\ \Delta\mathbf{w}_3 &= -2\Delta\beta, \end{aligned}$$

where we have dropped the recurring $i+1/2$ indices. Furthermore, with Chandrashekar's flux, $f^{\rho,C} = \hat{\rho}_{i+1/2}\bar{u}_{i+1/2}$, in place of f^ρ, and $f^{m,C}$ and $f^{E,C}$ given by (21), it was demonstrated that

$$f^{\rho,C}\Delta\mathbf{w}_1 + f^{m,C}\Delta\mathbf{w}_2 + f^{E,C}\Delta\mathbf{w}_3 = \Delta m = \bar{\rho}\Delta u + \bar{u}\Delta\rho, \tag{30}$$

and thus (29) is satisfied as an equality. (Chandrashekar's scheme is entropy conservative.)

Remark. We have verified all results in [3] that are used herein. △

Hence, (21) leads to entropy stability, if it is more diffusive than Chandrashekar's flux. That is, if

$$(f^\rho - f^{\rho,C})\Delta\mathbf{w}_1 + (f^m - f^{m,C})\Delta\mathbf{w}_2 + (f^E - f^{E,C})\Delta\mathbf{w}_3 \leq 0 \tag{31}$$

or

$$\begin{aligned} &(f^\rho - f^{\rho,C})\left(\frac{\Delta\rho}{\hat{\rho}} + \left(\frac{1}{(\gamma-1)\hat{\beta}} - \overline{u^2}\right)\Delta\beta - 2\bar{u}\bar{\beta}\Delta u\right) \\ &\qquad + (\bar{u}(f^\rho - f^{\rho,C}))(2\bar{\beta}\Delta u + 2\bar{u}\Delta\beta) \\ &+\left(\left(\frac{1}{2(\gamma-1)\hat{\beta}} - \frac{1}{2}\overline{u^2}\right)(f^\rho - f^{\rho,C}) + \bar{u}\bar{u}(f^\rho - f^{\rho,C})\right)(-2\Delta\beta) \leq 0. \end{aligned}$$

Cancellations leaves us with the following condition for entropy stability,

$$(f^\rho - f^{\rho,C})\left(\frac{\Delta\rho}{\hat{\rho}}\right) \leq 0. \tag{32}$$

Using (21), (22) and (17), we obtain

$$f^\rho - f^{\rho,C} = \bar{\rho}\bar{u} - \lambda^\rho\Delta\rho - \hat{\rho}\bar{u} = \bar{\rho}\bar{u} - (\frac{|\bar{u}|}{2} + \frac{|\Delta u|}{4})\Delta\rho - \hat{\rho}\bar{u}$$

which is inserted into the left-hand side of (32)

$$\left((\bar{\rho}-\hat{\rho})\bar{u}-(\frac{|\bar{u}|}{2}+\frac{|\Delta u|}{4})\Delta\rho\right)\frac{\Delta\rho}{\hat{\rho}}\leq 0$$

where the last inequality follows from $|\bar{\rho}-\hat{\rho}|\leq\frac{\Delta\rho}{2}$ since both $\hat{\rho}$ and $\bar{\rho}$ are monotone averages of positive quantities and hence the distance between the arithmetic mean and any other mean is at most $|\Delta\rho|/2$.

Next, we turn to the viscous terms. We need the identity,

$$\Delta\beta_{i+1/2}=\frac{1}{2R}\left(\frac{1}{T_{i+1}}-\frac{1}{T_i}\right)=-\frac{1}{2R}\frac{T_{i+1}-T_i}{T_{i+1}T_i}=-\frac{1}{2R}\frac{\Delta T_{i+1/2}}{T_{i+1}T_i}. \tag{33}$$

Inserting the expressions for $\Delta\mathbf{w}$, $\mathbf{f}^V$ and (33) into (28) results in,

$$\begin{aligned}\Delta\mathbf{w}^T\mathbf{f}^V=\Delta\mathbf{w}_2 f^{V2}+\Delta\mathbf{w}_3 f^{V3}=\\ (2\bar{\beta}\Delta u+2\bar{u}\Delta\beta)\tau_{xx}+(-2\Delta\beta)(\bar{u}\tau_{xx}+\kappa\frac{\Delta T}{h})=\\ (2\bar{\beta}\Delta u)\tau_{xx}+(-2\Delta\beta)(\kappa\frac{\Delta T}{h})=\\ \frac{8\mu}{3h}\bar{\beta}(\Delta u)^2+\frac{\kappa}{Rh}\frac{(\Delta T)^2}{T_{i+1}T_i}\geq 0\end{aligned}$$

where the last inequality follows from the assumption of positive temperature. When summed over the domain, the last two terms bound the discrete L^2 norms of $\frac{\sqrt{\bar{T}_{i-1/2}}}{\bar{T}_{i-1/2}}D_-u_i$ and $\frac{\sqrt{\kappa_{i-1/2}}}{\bar{T}_{i-1/2}}D_-T_i$. We have thus demonstrated that the entropy condition B is satisfied for the discrete scheme (20).

Finally, we consider Condition C. The discrete kinetic energy balance is obtained as

$$\begin{aligned}\frac{d}{dt}K_i=\left(-\frac{1}{2}u_i^2(\rho_i)_t+u_i(m_i)_t\right)=\\ -\frac{1}{2}u_i^2D_-(-f^\rho_{i+1/2})+u_iD_-(-f^m_{i+1/2}+f^{V2}_{i+1/2})=\\ -\frac{1}{4}(D_-u_{i+1}^2)f^\rho_{i+1/2}-\frac{1}{4}(D_-u_i^2)f^\rho_{i-1/2}+\frac{1}{2}D_-(\overline{u^2}_{i+1/2}f^\rho)_{i+1/2}\\ -\frac{1}{2}(D_-u_{i+1})(-f^m_{i+1/2}+f^{V2}_{i+1/2})-\frac{1}{2}(D_-u_i)(-f^m_{i-1/2}+f^{V2}_{i-1/2})\\ +D_-(\bar{u}_{i+1/2}(-f^m_{i+1/2}+f^{V2}_{i+1/2}))=\\ +\frac{1}{2}D_-(\overline{u^2}_{i+1/2}f^\rho)_{i+1/2}\\ +\frac{1}{2}(D_-u_{i+1})(\tilde{p}_{i+1/2}-\frac{4}{3}D_-u_{i+1})+\frac{1}{2}(D_-u_i)(\tilde{p}_{i-1/2}-\frac{4\mu}{3}D_-u_i)\\ +D_-(\bar{u}_{i+1/2}(-f^m_{i+1/2}+f^{V2}_{i+1/2})).\end{aligned}$$

Collecting terms results in the balance

$$\begin{aligned}\frac{d}{dt}K_i=&\frac{1}{2}\left((D_-u_{i+1})\tilde{p}_{i+1/2}+(D_-u_i)\tilde{p}_{i-1/2}\right)-\frac{4\mu}{3}\frac{(D_-u_{i+1})^2+(D_-u_i)^2}{2}\\ &+D_-\left((\frac{1}{2}\overline{u^2}_{i+1/2}-\bar{u}^2_{i+1/2})f^\rho-\bar{u}_{i+1/2}\tilde{p}_{i+1/2}+\bar{u}_{i+1/2}f^{V2}_{i+1/2}\right).\end{aligned}$$

Integrating the kinetic energy balance, would give a bound on velocity gradients, had we a sufficiently strong bound on pressure, which we do not. Another path forward is via the internal energy equation, which is why we demand kinetic energy preserving schemes. By perusing the kinetic energy balance above, it is clear that the convective and viscous terms are approximated exactly as in the total energy equation. Hence, subtracting the kinetic energy balance from the total energy balance gives the internal energy balance without any rest terms from velocity.

$$\begin{aligned}\partial_t(c_v\rho T)_i+D_-\left(\left(\frac{1}{2(\gamma-1)\hat{\beta}_{i+1/2}}\right)f^\rho-\kappa\frac{T_{i+1}-T_i}{h}\right)\\ +\frac{1}{2}\left((D_-u_{i+1})\tilde{p}_{i+1/2}+(D_-u_i)\tilde{p}_{i-1/2}\right)-\frac{4\mu}{3}\frac{(D_-u_{i+1})^2+(D_-u_i)^2}{2}=0.\end{aligned} \tag{34}$$

As mentioned above, the internal energy balance can be used to provide further estimates as in [6] and [7].

We have proven the following proposition.

Proposition 4.1. *The scheme (20), (21), (22) and (23), satisfies Conditions A-E.*

Remark. Although rarely addressed, standard turbulence models are not exempt from strong requirements (similar to Conditions A-E) since they too should ultimately be well-posed. △

4.1. 2-D equidistant finite volume scheme

The generalisation of the inviscid fluxes to 2-D (and 3-D) is trivial. As is the corresponding parts of the proofs. The viscous terms require more care and we refer to [19,16], and merely state the 2-D scheme here. The extension to 3-D follows the same pattern.

In 2-D, the domain is the periodic square with $N+1$ equidistant points in each direction. (Solution values at the end points are equal.) Throughout, the averages and differences defined in (16) are taken in different coordinate directions indicated by the "half" index. For instance, $\bar{a}_{ij+1/2} = \frac{a_{ij+1}+a_{ij}}{2}$.

The scheme is given as,

$$(\mathbf{u}_{ij})_t + \frac{\mathbf{f}_{i+1/2j} - \mathbf{f}_{i-1/2j}}{h} + \frac{\mathbf{g}_{ij+1/2} - \mathbf{g}_{ij-1/2}}{h} = 0 \tag{35}$$

where $\mathbf{u}_{ij} = (\rho_{ij}, \rho\mathbf{v}_{ij}, E_{ij})^T$, $E_{ij} = \frac{p_{ij}}{\gamma-1} + \frac{1}{2}\rho_{ij}|\mathbf{v}_{ij}|^2$ and $\mathbf{v}_{ij} = (u_{ij}, v_{ij})$.

As in the 1-D case, $\mathbf{f}$ and $\mathbf{g}$ consist of an inviscid and a viscous flux vector. Namely,

$$\begin{aligned}
f^{\rho}_{i+1/2j} &= \bar{\rho}_{i+1/2j}\bar{u}_{i+1/2j} - \lambda^{\rho}_{i+1/2j}\Delta\rho_{i+1/2j},\\
f^{m1}_{i+1/2j} &= \frac{\bar{\rho}_{i+1/2j}}{2\bar{\beta}_{i+1/2j}} + \bar{u}_{i+1/2j}f^{\rho}_{i+1/2j}\\
f^{m2}_{i+1/2j} &= \bar{v}_{i+1/2j}f^{\rho}_{i+1/2j},\\
f^{E}_{i+1/2j} &= \left(\frac{1}{2(\gamma-1)\hat{\beta}_{i+1/2j}} - \frac{1}{2}(\overline{u^2}_{i+1/2j} + \overline{v^2}_{i+1/2j})\right) f^{\rho}_{i+1/2j}\\
&\quad + \bar{u}_{i+1/2j}f^{m1}_{i+1/2j} + \bar{v}_{i+1/2j}f^{m2}_{i+1/2j},
\end{aligned} \tag{36}$$

and

$$\begin{aligned}
g^{\rho}_{ij+1/2} &= \bar{\rho}_{ij+1/2}\bar{v}_{ij+1/2} - \lambda^{\rho}_{ij+1/2}\Delta\rho_{ij+1/2}\\
g^{m1}_{ij+1/2} &= \bar{u}_{ij+1/2}g^{\rho}_{ij+1/2}\\
g^{m2}_{ij+1/2} &= \frac{\bar{\rho}_{ij+1/2}}{2\bar{\beta}_{ij+1/2}} + \bar{v}_{ij+1/2}g^{\rho}_{ij+1/2}\\
g^{E}_{ij+1/2} &= \left(\frac{1}{2(\gamma-1)\hat{\beta}_{ij+1/2}} - \frac{1}{2}(\overline{u^2}_{ij+1/2} + \overline{v^2}_{ij+1/2})\right) g^{\rho}_{ij+1/2}\\
&\quad + \bar{u}_{ij+1/2}g^{m1}_{ij+1/2} + \bar{v}_{ij+1/2}g^{m2}_{ij+1/2}.
\end{aligned}$$

Furthermore, the artificial viscosity coefficients are

$$\begin{aligned}
\lambda^{\rho}_{i+1/2j} &= \frac{|\bar{u}_{i+1/2j}|}{2} + \frac{|\Delta u_{i+1/2j}|}{4},\\
\lambda^{\rho}_{ij+1/2} &= \frac{|\bar{v}_{ij+1/2}|}{2} + \frac{|\Delta v_{ij+1/2}|}{4}.
\end{aligned} \tag{37}$$

The viscous fluxes are given by

$$\begin{aligned}
f^{V1}_{i+1/2j} &= 0,\\
f^{V2}_{i+1/2j} &= (\tau_{xx})_{ij},\\
f^{V3}_{i+1/2j} &= (\tau_{xy})_{ij},\\
f^{V4}_{i+1/2j} &= u_{i+1j}(\tau_{xx})_{ij} + v_{i+1j}(\tau_{xy})_{ij} + \bar{\kappa}_{i+1/2j}\frac{T_{i+1j} - T_{ij}}{h},
\end{aligned} \tag{38}$$

and

$$
\begin{aligned}
g^{V1}_{ij+1/2} &= 0 \\
g^{V2}_{ij+1/2} &= (\tau_{xy})_{ij} \\
g^{V3}_{ij+1/2} &= (\tau_{yy})_{ij} \\
g^{V4}_{ij+1/2} &= u_{ij+1}(\tau_{xy})_{ij} + v_{ij+1}(\tau_{yy})_{ij} + \bar{\kappa}_{ij+1/2}\frac{T_{ij+1}-T_{ij}}{h}
\end{aligned}
\tag{39}
$$

where

$$
\begin{aligned}
(\tau_{xx})_{i+1/2j} &= 2\mu(\mathfrak{u}_x)_{ij} - \frac{2\mu}{3}((\mathfrak{u}_x)_{ij} + (\mathfrak{v}_y)_{ij}) \\
(\tau_{xy})_{ij} &= \mu((\mathfrak{u}_y)_{ij} + (\mathfrak{v}_x)_{ij}) \\
(\tau_{yy})_{ij+1/2} &= 2\mu(\mathfrak{v}_y)_{ij} - \frac{2\mu}{3}((\mathfrak{u}_x)_{ij} + (\mathfrak{v}_y)_{ij})
\end{aligned}
$$

and

$$
\begin{aligned}
(\mathfrak{u}_x)_{ij} &= \frac{u_{i+1j}-u_{ij}}{h}; \quad (\mathfrak{v}_x)_{ij} = \frac{v_{i+1j}-v_{ij}}{h}; \\
(\mathfrak{u}_y)_{ij} &= \frac{u_{ij+1}-u_{ij}}{h}; \quad (\mathfrak{v}_y)_{ij} = \frac{v_{ij+1}-v_{ij}}{h}.
\end{aligned}
$$

Remark. The viscous approximation is not symmetric around (x_i, y_j) and therefore only first-order accurate. It is possible to make an entropy stable symmetric operator but it has no impact on our numerical results below since they are under-resolved anyway. △

5. Numerical simulations

We consider three different cases: 1) The 1-D Shu-Osher shock-entropy wave interaction. This is primarily included to demonstrate the shock-capturing properties of the proposed scheme. 2) A Kelvin-Helmholtz instability is used to study the continuity of initial conditions, i.e., the predictability of the scheme. As is well-known, this case has a high sensitivity to perturbations and instabilities are prone to be tripped by numerical errors. 3) A Taylor-Green vortex at $Re = 1600$. This is used to monitor the kinetic energy decay and enstrophy.

5.1. Shu-Osher shock-entropy wave interaction

The computational domain is $\Omega = (-5, 5)$ and the initial data is given by

$$
(\rho, u, p) = \begin{cases} (3.857143, 2.629369, 10.3333) & x < -4 \\ (1 + 0.2\sin(5x), 0, 1) & x \geq -4 \end{cases}
\tag{40}
$$

The initial data is also used as boundary data. In this case, $\gamma = 1.4$ and to extend it to the Navier-Stokes, we use $R = 287.15$ and $Pr = 0.72$. (Standard values for air in SI-units.) To have some viscous effects at reasonable grid resolutions, we use $\mu = 1e-2$. The semi-discrete scheme (20) was marched with the Euler forward scheme in time.

As is customary, we run the simulations till $\mathcal{T} = 2$ and display the results for density in Fig. 1. The purpose with this scheme is not to compete with methods more or less designed to resolve this case accurately. As a DNS scheme, the solution is wildly under-resolved with $N = 200$ points. Yet, it runs stably without any additional artificial diffusion at the strong shock. As discussed above we should not interpret the solution pointwise. (At this level of resolution.) Clearly, this is the case as the oscillations trailing the strong shock are not pointwise accurate and yet information is passing through the shock and the weak shocks trailing the strong shock are formed. The weak shocks are diffused, by both the artificial diffusion and the physical viscosity, but at the correct positions. (See the zoom in Fig. 1.)

As resolution increases, the trailing shocks are more resolved and the unresolved region behind the strong shock is decreasing. However, the solution will of course never completely approach the standard Euler solution since physical diffusion is added. Furthermore, we point to a remarkable feature of the scheme that is due to the particular artificial diffusion: there is no undershoot at the strong shock *even in the inviscid case* ($\mu = 0$).

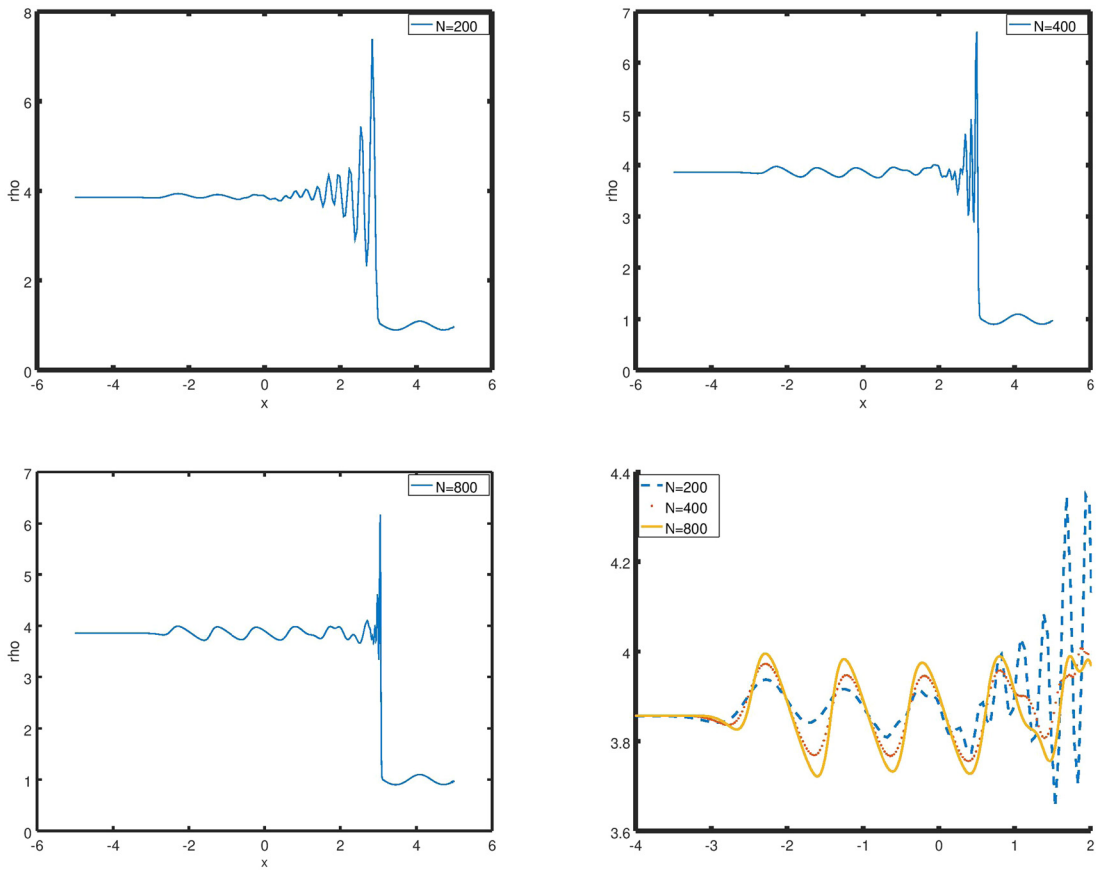

Fig. 1. The density solution of the Shu-Osher case at $T = 2$.

5.2. Kelvin-Helmholtz instability

We run the same case as in [20]. The domain is $(x, y) \in (0, 1) \times (0, 1)$ and periodic in both directions. The initial conditions are given by

$$\mathbf{u}(x, y, t = 0) = \begin{cases} \mathbf{u}^1 & 0.25 < y < 0.75 \\ \mathbf{u}^2 & y \leq 0.25 \text{ or } y \geq 0.75 \end{cases} \tag{41}$$

where

$$\begin{aligned} \rho^1 = 1, \quad \rho^2 = 2 \\ u^1 = -0.5 + \epsilon \sin(2\pi x), \quad u^2 = 0.5 + \epsilon \sin(2\pi x) \\ v^1 = v^2 = \epsilon \sin(2\pi y) \\ p^1 = p^2 = 2.5 \end{aligned}$$

and $\epsilon = 0.1$. The ϵ-perturbation trips the instability and produces the familiar rolls. The problem is solved on Cartesian equidistant grids with N^2 points in space and the timestep $0.004h$. The Euler forward scheme was used to march in time.

The solution to this problem is a single roll in the upper half and another one in the lower half of the domain. The initial conditions lack any other perturbations that could induce other rolls. Hence, when the perturbation is resolved, the double roll is the only structure we should observe.

However, the scheme (35) can not distinguish between (41) and initial data with perturbations of shorter wave lengths than those resolved on the grid. Hence, the scheme should produce a weak solution whose mean value is approximately correct in a neighbourhood of a point irrespective of there being unresolved perturbations or not. That is, it should be slightly diffused. (What it should *not* do is allow numerical errors to trip instabilities, since that would violate the assumption of continuity of input data.)

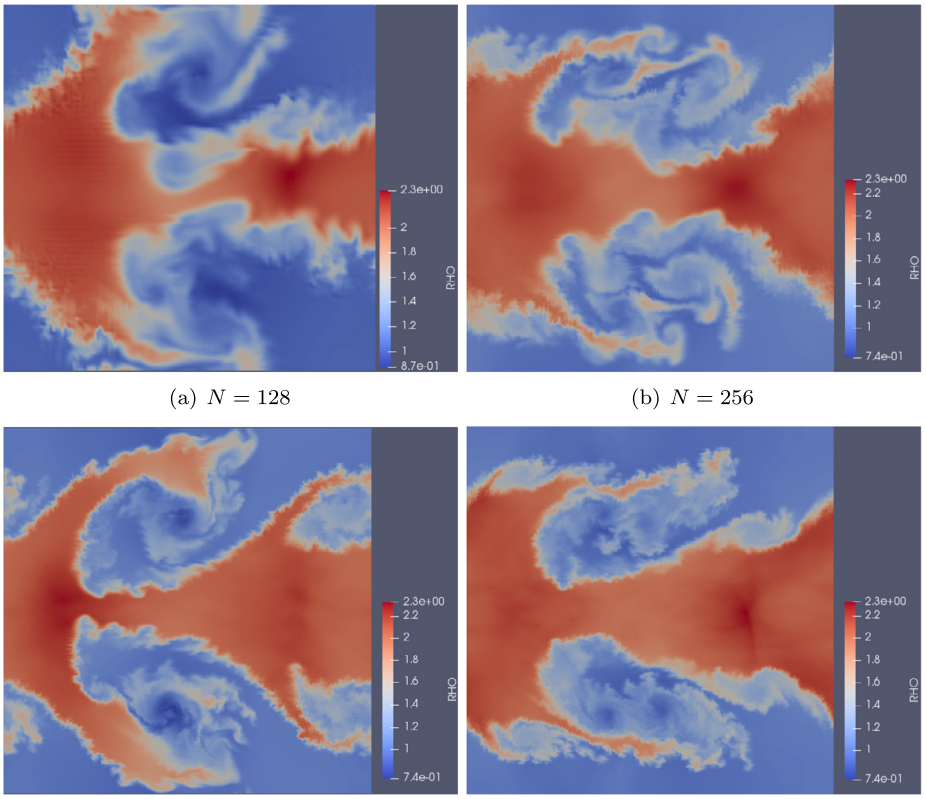

(a) $N = 128$ (b) $N = 256$

(c) $N = 512$ (d) $N = 1024$

Fig. 2. Solution of Euler equations, i.e. (35) computed with the fluxes given in Section 4.1 and with $\mu = \kappa = 0$. (For interpretation of the colours in the figure(s), the reader is referred to the web version of this article.)

Turning to the numerical experiments, we begin with some qualitative observations. First, we consider the numerical solution of the Euler equations obtained by (35) with $\mu = \kappa = 0$. In this case, only density is checked by diffusion and we should expect spurious rollers to appear due to linear instabilities in velocity and/or temperature. Indeed, that seems to be the case as seen in Fig. 2.

By setting $\kappa = \mu = 1e-4$ a completely different behaviour is obtained, as seen in Fig. 3. Due to under-resolution, the physical diffusion is not sufficient to control linear instabilities and prevent unphysical roll-ups on the coarsest grid as seen in Fig. 3(a). However, a further grid refinement prevents unphysical roll-ups, since the second derivatives in the diffusive terms scale as h^{-2} such that they dominate the linearly unstable terms on sufficiently fine meshes. (See Fig. 3(b).)

To further investigate the property of local linear stability, we replace ($\mathbf{f}^\rho$ and $\mathbf{g}^\rho$ by Chandrashekar's fluxes $\mathbf{f}^{\rho,C}_{i+1/2j} = \hat{\rho}_{i+1/2j}\bar{u}_{i+1/2j}$ and $\mathbf{g}^{\rho,C} = \hat{\rho}_{ij+1/2}\bar{v}_{ij+1/2j}$ (and $\mu = \kappa = 1e-4$). In this case, the continuity equation is not linearly stable ([10]). The results are displayed in Fig. 4. The physical viscosity is exerting a significant control of small scale roll-ups compared with Fig. 2 but less so than the proposed scheme in Fig. 3 and a finer grid is required to obtain a good approximation.

Finally, we have run the case with $\mu = \kappa = 0$ (the Euler equations) and the following inviscid fluxes.

$$
\begin{aligned}
\mathbf{f}^{\rho}_{i+1/2j} &= \bar{\rho}_{i+1/2j}\bar{u}_{i+1/2j} - \lambda^{\rho}_{i+1/2j}\Delta\rho_{i+1/2j},\\
\mathbf{f}^{m1}_{i+1/2j} &= \frac{\bar{\rho}_{i+1/2j}}{2\hat{\beta}_{i+1/2j}} + \bar{u}_{i+1/2j}\bar{\rho}_{i+1/2j}\bar{u}_{i+1/2j} - \lambda^{\rho}_{i+1/2j}\Delta(\rho u)_{i+1/2j}\\
\mathbf{f}^{m2}_{i+1/2j} &= \bar{v}_{i+1/2j}\bar{\rho}_{i+1/2j}\bar{u}_{i+1/2j} - \lambda^{\rho}_{i+1/2j}\Delta(\rho v)_{i+1/2j},\\
\mathbf{f}^{E}_{i+1/2j} &= \left(\frac{1}{2(\gamma-1)\hat{\beta}_{i+1/2j}} - \frac{1}{2}(\overline{u^2}_{i+1/2j} + \overline{v^2}_{i+1/2j})\right)\bar{\rho}_{i+1/2j}\bar{u}_{i+1/2j}\\
&\quad + \bar{u}_{i+1/2j}\mathbf{f}^{m1}_{i+1/2j} + \bar{v}_{i+1/2j}\mathbf{f}^{m2}_{i+1/2j} - \lambda^{\rho}_{i+1/2j}\Delta E_{i+1/2j},
\end{aligned}
\tag{42}
$$

and

$$
\mathbf{g}^{\rho}_{ij+1/2} = \bar{\rho}_{ij+1/2}\bar{v}_{ij+1/2} - \lambda^{\rho}_{ij+1/2}\Delta\rho_{ij+1/2}
$$

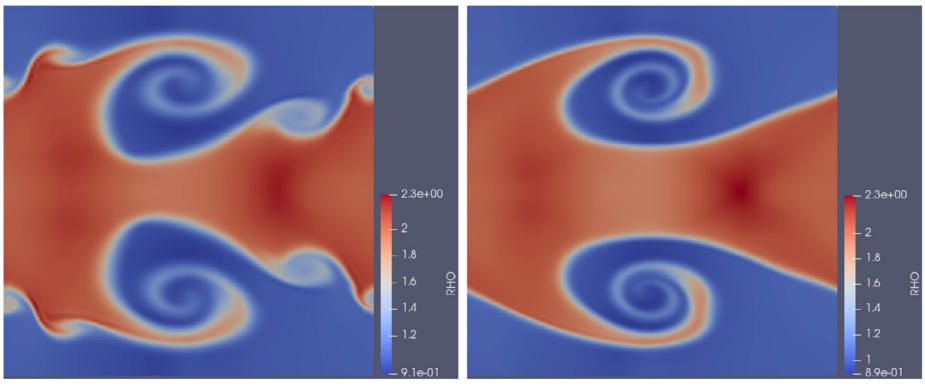

(a) $N = 128$ (b) $N = 256$

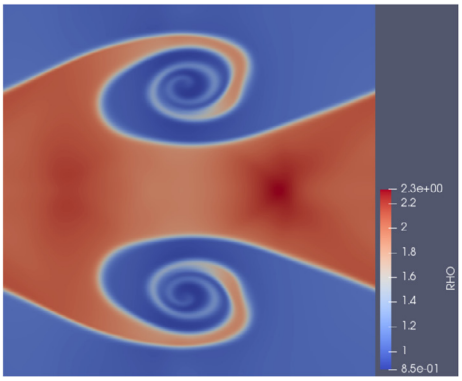

(c) $N = 512$

Fig. 3. The Navier-Stokes equations solved with the scheme (35) along the fluxes given in Section 4.1 with $\mu = \kappa = 1e-4$.

Table 1
The $\mathbb{B}$-means computed with the scheme (35) with $\mu = \kappa = 1e-4$.

N=	128	256	512
$\bar{\rho}$	2.036	1.985	2.000
$\overline{\rho u}$	0.193	0.217	0.212
$\overline{\rho v}$	0.378	0.361	0.365
$\bar{E}$	9.361	9.190	9.242

$$
\begin{aligned}
\mathbf{g}^{m1}_{ij+1/2} &= \bar{u}_{ij+1/2}\overline{\rho v}_{ij+1/2} - \lambda^{\rho}_{ij+1/2}\Delta(\rho u)_{ij+1/2} \\
\mathbf{g}^{m2}_{ij+1/2} &= \frac{\bar{\rho}_{ij+1/2}}{2\bar{\beta}_{ij+1/2}} + \bar{v}_{ij+1/2}\bar{\rho}_{ij+1/2}\bar{v}_{ij+1/2} - \lambda^{\rho}_{ij+1/2}\Delta(\rho v)_{ij+1/2} \\
\mathbf{g}^{E}_{ij+1/2} &= \left(\frac{1}{2(\gamma-1)\hat{\beta}_{ij+1/2}} - \frac{1}{2}(\overline{u^2}_{ij+1/2} + \overline{v^2}_{ij+1/2})\right)\bar{\rho}_{ij+1/2}\bar{v}_{ij+1/2} \\
&\quad + \bar{u}_{ij+1/2}\mathbf{g}^{m1}_{i+1/2j} + \bar{v}_{ij+1/2}\mathbf{g}^{m2}_{i+1/2j} - \lambda^{\rho}_{ij+1/2}\Delta E_{ij+1/2}.
\end{aligned}
\tag{43}
$$

That is, compared with (35), the artificial diffusion is removed from f^{ρ}/g^{ρ} and instead added to every variable in the respective directions. The results are shown in Fig. 5 and the diffusion seems to enforce linear stability as no spurious roll-ups appear, but it is significantly more diffusive than the proposed scheme in Fig. 3.

Next, we turn to quantitative comparisons. The fundamental idea of this paper is that weakly convergent solutions can be understood as LES-like averages on finite (ideally coarse) grids. To test this, we define the square $\mathbb{B} = [0.2, 0.4] \times [0.5, 0.7]$. The mean of the primary variables inside $\mathbb{B}$ are computed for the different cases discussed above. The location of $\mathbb{B}$ is chosen such that it encompasses parts of both layers. The size is chosen such that even on the coarsest grid, $N = 128^2$, there are 26 points along each side of $\mathbb{B}$, which would suggest that the mean should be well-resolved. (We stress that $\mathbb{B}$ has not been subject to any "tuning". This is the only box tested.)

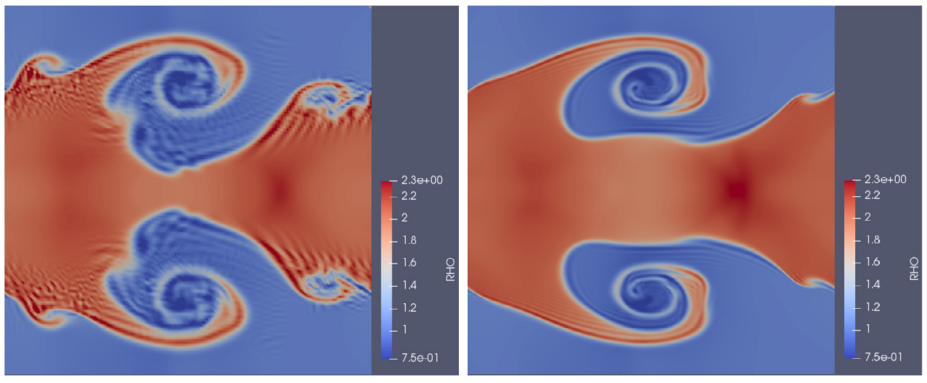

(a) $N = 128$ (b) $N = 256$

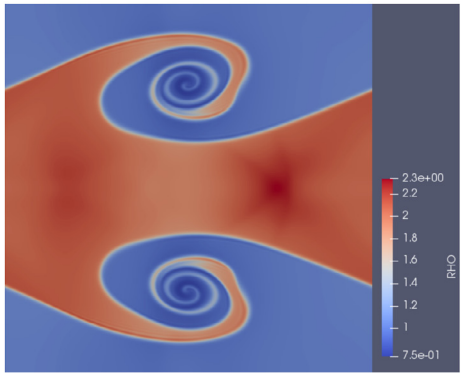

(c) $N = 512$

Fig. 4. Navier-Stokes equations solved with Chandrashekar's flux and $\mu = \kappa = 1e-4$.

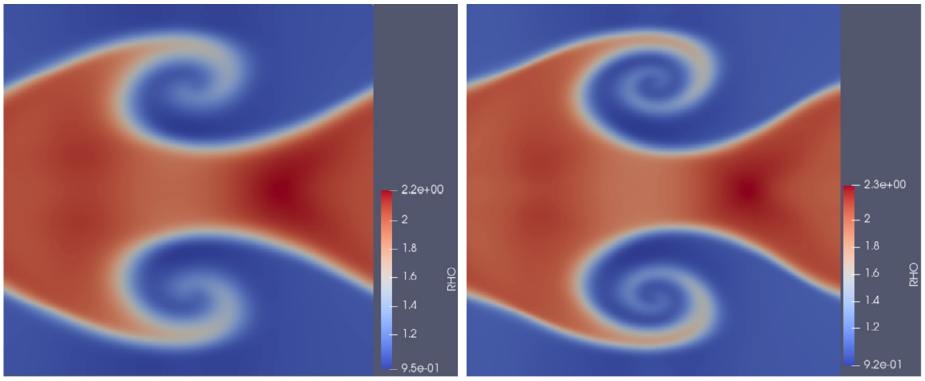

(a) $N = 128$ (b) $N = 256$

Fig. 5. Euler with artificial diffusion on all variables. (The fluxes (42) and (43) with $\lambda^\rho = \overline{|\mathbf{u}\cdot\mathbf{n}|}/2 + \Delta(\mathbf{u}\cdot\mathbf{n})/4$).

In Table 1, the $\mathbb{B}$-mean values for the Navier-Stokes solution, i.e., (35) with $\mu = \kappa = 1e-4$, for three different grid resolutions are shown. (Corresponding to Fig. 3.) The difference between the coarsest and the finest grid is less than 10% in all variables and the averages appear to be converging.

Remark. The point here is not to demonstrate strong or pointwise convergence to a grid converged solution. We want to demonstrate the idea put forth in this paper. Namely, it might be possible to evaluate the accuracy of a functional even on coarse meshes and that this functional might be reasonably accurate even if the solution is far from being grid converged. What grid resolution that is required will of course depend on the problem, the functional of interest and the accuracy requirement.

Table 2
The $\mathbb{B}$-means computed with the scheme (35) with $\mu = \kappa = 0$ (Euler).

N=	128	256	512	1024
$\bar{\rho}$	2.603	1.830	1.988	1.851
$\overline{\rho u}$	0.128	0.175	0.230	0.283
$\overline{\rho v}$	0.627	0.275	0.400	0.257
$\bar{E}$	9.658	8.968	9.090	8.926

Table 3
The $\mathbb{B}$-means computed with Chandraskekar's entropy and kinetic energy preserving flux, with $\mu = \kappa = 1e-4$.

N=	128	256	512
$\bar{\rho}$	2.075	1.975	1.993
$\overline{\rho u}$	0.192	0.223	0.215
$\overline{\rho v}$	0.415	0.363	0.366
$\bar{E}$	9.426	9.196	9.240

Table 4
The $\mathbb{B}$-means computed for the Euler equations solved with the scheme (42)-(43).

N=	128	256
$\bar{\rho}$	2.206	2.112
$\overline{\rho u}$	0.140	0.157
$\overline{\rho v}$	0.365	0.395
$\bar{E}$	9.398	9.224

The $\mathbb{B}$-mean values for the Euler solutions (corresponding to Fig. 2) are displayed in Table 2. First, we note that although yet another refinement has been carried out, it would be a stretch to claim that these values are on a convergent path. They are of course not completely off in comparison with the values in Table 1, but even the fine grid solution is off by 33% and 42% in the momentum variables in relation to the finest grid values in Table 1.

Turning to the simulations resulting in Fig. 4, where Chandrashekar's flux and $\mu = \kappa = 1e-4$ are used, we obtain the means shown in Table 3. On the finest mesh, where the linear instabilities are handled by the scheme, the relative differences to Table 1, are less than 1%. However, the relative difference in density between the coarsest and the finest grid is 1.8% for the scheme (35)/Table 1 and 4.1% in Table 3. This supports the idea that local stability improves results on coarse meshes.

Finally, we turn to the means for the Euler scheme (42)-(43) presented in Table 4. Here, the extra artificial diffusion smears the transition. The smearing should be interpreted as an uncertainty of the behaviour in the transition region regarding instabilities with short wave lengths. However, the scheme leans towards being overly cautious, which makes the scheme less accurate than (35).

5.2.1. Discussion of the Kelvin-Helmholtz results

It is clear that numerical errors trip a multitude of instabilities in the Euler solutions computed with (35) and $\mu = \kappa = 0$. (One can view this case as a very under-resolved Navier-Stokes simulation where the viscosity has negligible effect.) The very detailed structures may be interpreted as a token of the fidelity of the simulation. However, the $\mathbb{B}$-means reveal that the "high-fidelity" solutions in Fig. 2 are the *least* accurate and caused by amplifications of random numerical errors.

This demonstrates that what may look like turbulent features in under-resolved simulations may be unphysical numerical errors amplified by the scheme. It should also be emphasised that the simulations in Fig. 2 are highly grid and scheme dependent making them essentially non-predictive.

The proposed scheme is clearly not perfect either. On the coarsest grid ($N = 128$) there are spurious rollers due to insufficient diffusion which allows linear instabilities to grow. Despite this, the $\mathbb{B}$-means are still fairly accurate since the large scale structures are reasonably captured. However, the instabilities are removed with a finer grid and there is clearly convergence. This provides a way to estimate the accuracy by monitoring the convergence of functionals.

The Chandrashekar flux with the Navier-Stokes viscosity, still allows linear instabilities in the continuity equation to grow. However, they seem to be damped by the physical diffusion, albeit at finer grids. This is also reflected in the $\mathbb{B}$-means that do converge.

Finally, when the Euler equations are subject to first-order diffusion in all variables linear stability is recovered for the tested grids. However, the scheme is a fair bit more diffusive, which is manifested as less accurate $\mathbb{B}$-means. Furthermore, in the next problem, the Taylor-Green vortex, it does not damp vorticity and kinetic energy at any reasonable rate, since it lacks physical diffusion. Hence, we will not consider it further.

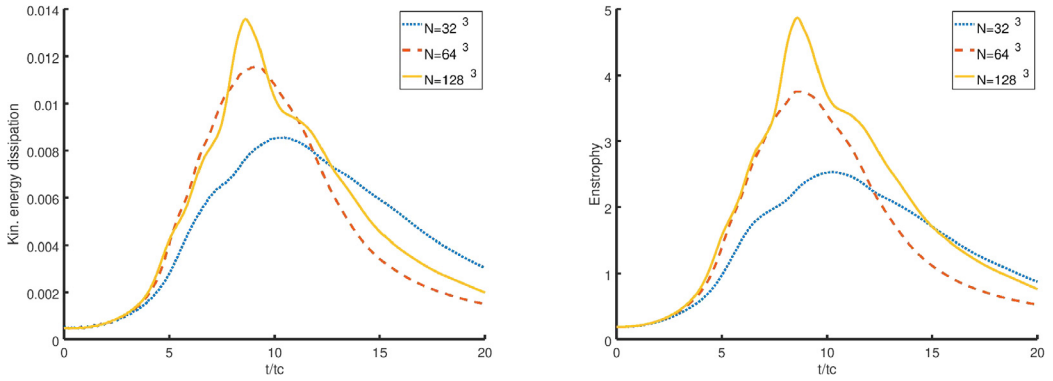

(a) Kinetic energy dissipation (b) Enstrophy

Fig. 6. Taylor-Green vortex at $Re = 1600$.

Based on this problem, the proposed entropy dissipative Navier-Stokes scheme (35) seems to strike a balance between excessive diffusion and too little diffusion, although one should still interpret the results with caution. Grid refinements are necessary to evaluate its accuracy for any given problem.

5.3. Taylor-Green vortex at Re=1600

This is a standard test for evaluating the capability of a scheme to approximate turbulence. The domain $\Omega = -\pi L \leq x, y, z \leq \pi L$ is periodic and $L = 1$. It is discretised with a uniform mesh with $N = 32^3$, $N = 64^3$ and $N = 128^3$.

The initial data is given by,

$$u = V_0 \sin(\frac{x}{L}) \cos(\frac{y}{L}) \sin(\frac{z}{L})$$
$$v = -V_0 \cos(\frac{x}{L}) \sin(\frac{y}{L}) \sin(\frac{z}{L})$$
$$p = p_0 + \frac{\rho_0 V_0^2}{16} \left(\cos(\frac{2x}{L} + \cos(\frac{2y}{L}) \right) \left(\cos(\frac{2z}{L} + 2) \right)$$
$$\rho = \frac{p}{RT_0}$$

The Prandtl number is 0.71 and $\gamma = 1.4$. The bulk viscosity is assumed to be zero. Furthermore, $\rho_0 = 1$, $T_0 = 273.15$, and $R = 287.15$ and the Mach number is $M = 0.1 = V_0/c_0$, where c_0 is the speed of sound; $Re = \rho_0 V_0 L/\mu = 1600$ and $p_0 = \rho_0 R T_0$. The convective timescale is defined as $t_c = L/V_0$ and we run the simulations till $t_{final} = 20 t_c$. The time step is calculated as, $\Delta t = CFL \cdot h/(c_0 + |u_0|)$, and the scheme (35) (having been extended to 3-D) is marched in time using the Euler forward method.

The normalised kinetic energy is defined as

$$E_k = \frac{1}{\rho_0 |\Omega| V_0^2} \int_\Omega \rho \frac{|\mathbf{v}|^2}{2} d\Omega \tag{44}$$

where $|\Omega|$ is the measure of the volume. (All integrals are approximated using the trapezoidal rule.) The dissipation of the kinetic energy is,

$$\epsilon = -t_c \frac{dE_k}{dt} \tag{45}$$

which is approximated by a simple two-point backward difference in time. The enstrophy is given as,

$$\mathcal{E} = \frac{t_c^2}{\rho_0 |\Omega|} \int_\Omega \rho \frac{\omega \cdot \omega}{2} d\Omega \tag{46}$$

where $\omega = \nabla \times \mathbf{v}$ is the vorticity. The time evolutions of the kinetic-energy dissipation and the enstrophy, computed with the 3-D version of the scheme (35) on three different grids, are shown in Fig. 6.

The same case was run in [22]. There, for the best approximation, the maximal kinetic energy dissipation occurs at $t_c \approx 9$ and it is close to 0.0013. The maxima of the current (first-order) scheme are shown in Table 5. In [22], the second-order

Table 5
Maximum kinetic energy dissipation and occurrence in time for the three different grids.

N	max	t
32	0.008551	10.451
64	0.011565	9.0722
128	0.013569	8.6238

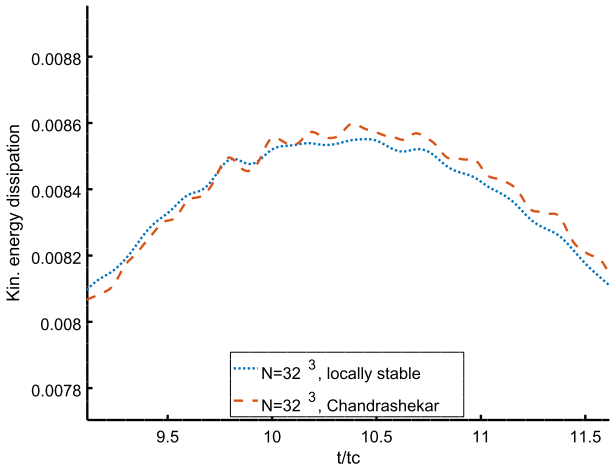

Fig. 7. Kinetic energy dissipation. Chandrashekar's flux in comparison with the locally stable scheme (35).

129^3 solution peaks at ≈ 0.0115 at $t_c \approx 8.3$. The current scheme is therefore significantly more accurate than the second-order scheme in [22] with respect to kinetic energy dissipation since it has the same peak with only 64 points and it is more accurate in time.

The same conclusion can be drawn for the enstrophy as well. The second-order scheme in [22] with 65^3 and 129^3 peaks at $\mathcal{E} \leq 2$ $\mathcal{E} \leq 4$, while the corresponding values for the current scheme are $\mathcal{E} \approx 4$ and $\mathcal{E} \approx 5$, which are closer to the reference that peaks at $\mathcal{E} \approx 10.3$.

The same simulations with Chandrashekar's scheme yield very similar results. This is not surprising since the flow is supposed to break down into turbulence and the linear instabilities therefore do not cause any "spurious turbulence". However, the effect of the locally unstable continuity equation is visible in Fig. 7 where Chandrashekar's flux has a more oscillatory behaviour.

6. Conclusions

In this paper, we have investigated the question if approximations of weak solutions on under-resolved grids can be interpreted as LES approximations. This led us to conjecture a number of conditions (A-E) that are necessary (albeit not sufficient) to define a weak solution in the first place and we derived a scheme satisfying these conditions.

Furthermore, well-posedness require continuity of data which demands that weakly convergent numerical solutions are scheme and grid independent. Hence, we require that numerical errors do not amplify and ruin the convergence of the averages.

The numerical experiments demonstrated that the proposed scheme (35) approximating the Navier-Stokes equations is stable in the presence of strong shocks and that the convergence of the averages for both the Kelvin-Helmholtz and Taylor-Green problem indicate that the scheme converges (at least) weakly.

Moreover, the plots in Fig. 2 display the emergence of unphysical fine-scale structures, that are not caused by the well-resolved initial conditions, when the scheme is not linearly stable. (This is consistent with and provides further support to the results in [10].) For the Navier-Stokes equations, these simulations are representative for solutions where the physical viscosity has no effect due to the coarseness of the grid and are thus effectively linearly unstable.

By considering the solutions as weakly convergent approximations, one should expect that averages taken over large parts of the domain converge faster than more local averages. (The fundamental principle of continuity of data, is hence with respect to weak averages, not point values.) This allows for accurate functional approximations on coarser grids and provides a mechanism for probing the accuracy (by a grid refinement). This idea has been corroborated by the numerical experiments and the proposed scheme (35) performs as expected.

We have likened this procedure to LES and we will end with a few remarks on that. In LES the filtering is done a priori. Upon convergence, a solution that does not contain the full range of eddies is obtained. For our scheme, a main difference

is that the filtering is done a posteriori, but like LES it does not provide information of under-resolved eddies. (Point-values are not necessarily accurate.) It also resembles ILES (and vanishing LES) since the range of resolved eddies is increasing with numerical resolution and the DNS solution is the ultimate target. The benefit of our method is that it offers a way to unify the prevailing theory for shock-capturing schemes and turbulence simulations.

CRediT authorship contribution statement

Magnus Svärd did all the work.

Declaration of competing interest

The authors declare that they have no known competing financial interests or personal relationships that could have appeared to influence the work reported in this paper.

References

[1] N.A. Adams, S. Hickel, Implicit Large-Eddy Simulation: theory and application, in: B. Eckhardt (Ed.), Advances in Turbulence XII, in: Springer Proceedings in Physics, vol. 132, Springer-Verlag, Berlin Heidelberg, 2009.
[2] M.H. Carpenter, T.C. Fisher, E.J. Nielsen, M. Parsani, M. Svärd, N. Yamaleev, Entropy stable summation-by-parts formulations for compressible computational fluid dynamics, in: R. Abgrall, C.W. Shu (Eds.), Handbook of Numerical Analysis, Vol. 17, chapter 10, Elsevier, 2016, pp. 495–524.
[3] P. Chandrashekar, Kinetic energy preserving and entropy stable finite volume schemes for compressible Euler and Navier-Stokes equations, Commun. Comput. Phys. 14 (5) (2013) 1252–1256.
[4] L.C. Evans, Partial Differential Equations, American Mathematical Society, 1998.
[5] T.C. Fisher, M.H. Carpenter, High-order entropy stable finite difference schemes for nonlinear conservation laws: finite domains, J. Comput. Phys. 252 (2013) 518–557.
[6] E. Feireisl, T. Karper, A. Novotný, A convergent numerical method for the Navier–Stokes–Fourier system, IMA J. Numer. Anal. 36 (2016) 1477–1535.
[7] E. Feireisl, M. Lukáčová-Medviďova, H. Mizerová, B. She, On the convergence of a finite volume method for the Navier-Stokes-Fourier system, IMA J. Numer. Anal. draa060 (2020).
[8] E. Feireisl, A. Novotný, Singular Limits in Thermodynamics of Viscous Fluids, 2nd ed, Birkhäuser, 2017.
[9] M. Germano, U. Piomelli, P. Moin, W.H. Cabot, A dynamic subgrid-scale eddy viscosity model, Phys. Fluids A, Fluid Dyn. 3 (7) (1991) 1760–1765.
[10] G. Gassner, M. Svärd, F. Hindenlang, Stability issues of entropy-stable and/or split-form high-order schemes. under review, J. Sci. Comput. (2020).
[11] T.J.R. Hughes, L.P. Franca, M. Mallet, A new finite element formulation for computational fluid dynamics: I. Symmetric forms of the compressible Euler and Navier-Stokes equations and the second law of thermodynamics, Comput. Methods Appl. Mech. Eng. (1986) 223–234.
[12] F. Ismail, P.L. Roe, Affordable, entropy-consistent euler flux functions II: entropy production at shocks, J. Comput. Phys. (2009) 5410–5436.
[13] M.P. Martin, U. Piomelli, G.V. Candler, Subgrid-scale models for compressible large-eddy simulations, Theor. Comput. Fluid Dyn. 13 (2000) 361–376.
[14] A.L. Marsden, O.V. Vasilyev, P. Moin, Construction of commutative filters for LES on unstructured meshes, J. Comput. Phys. 175 (2002) 584–603.
[15] Stephen B. Pope, Ten questions concerning the large-eddy simulation of turbulent flows, New J. Phys. 6 (35) (2004).
[16] M. Svärd, M.H. Carpenter, M. Parsani, Entropy stability and the no-slip wall boundary condition, SINUM 56 (1) (2018) 256–273.
[17] D. Serre, Systems of Conservation Laws, 1, Cambridge University Press, Cambridge, 1999.
[18] J. Simon, Compact sets in the space $l^p(o,t;b)$, Ann. Mat. Pura Appl. 146 (1986) 65–96.
[19] M. Svärd, A convergent numerical scheme for the compressible Navier– Stokes equations, SIAM J. Numer. Anal. 54 (3) (2016) 1484–1506.
[20] M. Svärd, Entropy solutions of the compressible Euler equations, BIT Numer. Math. 56 (4) (2016) 1479–1496.
[21] E. Tadmor, Entropy stability theory for difference approximations of nonlinear conservation laws and related time-dependent problems, Acta Numer. (2003) 451–512.
[22] E. van der Weide, G. Giangaspero, M. Svärd, Efficiency benchmarking of an energy stable high-order finite difference discretization, AIAA J. 53 (7) (2015).